Influence of Feature Size, Film Thickness, and Silicon Doping on the Performance of Nanostructured Hematite Photoanodes for Solar Water Splitting

Ilkay Cesar,[†,‡] Kevin Sivula,[†,*] Andreas Kay,[†] Radek Zboril,[§] and Michael Grätzel[†]

Institut des sciences et ingénierie chimiques, Ecole Polytechnique Fédérale de Lausanne, CH-1015 Lausanne, Switzerland, and Department of Physical Chemistry, Palacky University, Olomouc 77146, Czech Republic

Received: October 13, 2008; Revised Manuscript Received: November 11, 2008

Photoanodes consisting of nanostructured hematite prepared by atmospheric pressure chemical vapor deposition (APCVD) have previously set a benchmark for solar water splitting. Here, we fully investigate this promising system by varying critical synthetic parameters and probing the photoanode performance to determine the major factors that influence operation. By varying the film thickness, we show film growth to be linear with an incubation time. We find no concern with electron transport for films up to 600 nm, but a higher recombination rate of photogenerated carriers in the hematite near the interface with the fluorine-doped tin oxide, as compared to the bulk section of the film. The mechanism for the formation of the thin film's nanoporous dendritic structure is discussed on the basis of the results from varying the substrate growth temperate. The observed feature sizes of the film are found to depend strongly on this temperature and the presence of silicon dopant precursor (TEOS). Raman and Mössbauer experiments reveal how temperature and doping affect the crystallinity and ultimately the photoperformance. We also use impedance spectroscopy to find evidence for an unusually high donor density, which allows the formation of a space-charge field inside the nanosized features of the polycrystalline hematite photoanode.

1. Introduction

The efficient production of hydrogen from sunlight through the direct photo electrolysis of water over a photocatalyst is a promising route to the storage of sustainable energy. This method was first demonstrated in the advent of the oil crisis in 1972 by Fujishima and Honda.[1] Here, an n-type semiconductor photoelectrode in contact with an aqueous electrolyte solution is illuminated, producing electron−hole pairs. Because of the space-charge field in the semiconductor, the photo generated carriers separate. The holes migrate to the surface of the semiconductor to oxidize water (producing O_2), while the electrons travel through a circuit to a platinum counter electrode where they can reduce water to produced hydrogen (H_2). Because Fujishima et al. used TiO_2 with a band gap of 3.2 eV as the photoanode material, their device was only sensitive to 0.5% of the solar spectrum and had little prospect to become a viable means for solar hydrogen production.

Since this seminal demonstration, the search for the ideal water splitting semiconductor electrode has tapped many materials; however, the ideal material combining stability with the appropriate band gap and edge positions as compared to the reduction and oxidation potentials of water has not yet been found. However, α-Fe_2O_3 (hematite) remains a promising material. With a favorable band gap of 2.0−2.2 eV, chemical stability in aqueous environments, and matchless abundance, its use as a photocatalyst at a scale corresponding to the world energy demand is realistic. As a drawback, hematite possesses a conduction band edge at an energy level below the reversible hydrogen potential. Thus, an external electrical bias is required

to bring about the desired hydrogen evolution. However, by also using the solar photons with energy less than the band gap of hematite, unassisted solar hydrogen production can be achieved in a tandem cell configuration.[2] The theoretical maximum solar to chemical energy conversion efficiency of a hematite photoanode in such a tandem cell is 20%;[3] nevertheless, this has been far from realized due to the material's high rate of carrier recombination and poor charge transport characteristics.

The challenges set by this material are clearly illustrated by comparing its hole diffusion length, estimated to be between 2 and 4 nm,[4] to that of TiO_2, where values between 100 and 1000 nm are common.[4,5] However, decent performance has been obtained with carefully controlled materials. For example, monochromatic incident photon to electron conversion efficiencies (IPCE) for hematite of up to 37% (370 nm, 1 mW cm^{-2}, and 0.2 V vs SCE at pH 14) have been obtained for water splitting with single crystals doped with niobium.[6] Unfortunately, such crystals are expensive to create and not translucent, making them less suitable for mass production of solar hydrogen in a tandem cell. Much work has been reported on equally non-translucent pellets of sintered hematite powders with both n-type[7,8] and p-type[9] doping. Although that work contributed to a deeper understanding, quantum conversion efficiencies obtained did not match that of single crystals. Charge separation in these electrodes was typically interpreted in classical terms, driven by an electric field in the space-charge layer that develops in the semiconductor at the electrolyte interface (Schottky contact).[10,11] In n-type semiconductors, this space-charge layer is created by depletion of electrons as the semiconductor equilibrates with the redox potential of the electrolyte. The dominant factor that determines the photoresponse in such films is the match between the absorption depth of photons and the film thickness over which the space-charge electric field extends as electron−hole pairs generated in this layer are separated with

* To whom correspondence should be addressed. E-mail: kevin.sivula@epfl.ch.
† Ecole Polytechnique Fédérale de Lausanne.
‡ Current address: Energy research Centre of The Netherlands.
§ Palacky University.

Nanostructured Hematite Photoanodes

J. Phys. Chem. C, Vol. 113, No. 2, 2009 **773**

high efficiency.[12] The space-charge layer can typically develop over 30−300 nm in hematite electrodes for donor densities between 10^{19} and 10^{17} cm^{-3}.[11,13,14] In addition, holes that are photogenerated outside this layer can diffuse into this field and can contribute to the photocurrent. However, as the hole diffusion length of hematite is much smaller (<5 nm) than the width of the space-charge layer, little contribution to the photocurrent is expected from this diffusion layer.[15] Unfortunately, the majority of the solar photons in the wavelength range of 450−610 nm are absorbed by hematite via an indirect band gap transition. As these photons have long absorption depth, most holes are generated outside the electric field and recombine with electrons.[12,16,17] To alleviate this problem, it has been proposed to stack several electrodes with layer thicknesses comparable to the width of the space-charge layer. In such a way, the total light absorption is determined by the number of stacked electrodes, while the majority of photons are absorbed within the electric field of each electrode, enabling more holes to reach the surface to participate in the oxidation of water as compared to a single thick electrode.[12,18,19] Over the past decade, nanostructuring approaches have emerged to increase the semiconductor−electrolyte interfacial area. Nominally, if holes are always photogenerated throughout the electrode at a distance from the electrolyte smaller than their diffusion length, and a continuous electron transport path to the external circuit is present, sustainable charge separation and water oxidation can be completed in the absence of a space-charge electric field. Electrode designs based on this approach have been prepared using interconnected nanospheres[20] and perpendicular oriented nanorod arrays[21] of hematite on conducting SnO$_2$, but so far with limited water splitting efficiencies, photocurrent densities being in the μA cm^{-2} range at 1 sun and using 0.1 M NaOH electrolyte.[21]

Recently, silicon-doped hematite photoanodes prepared in our laboratory have demonstrated the potential of the nanostructuring approaches by showing improved photoresponse as the feature size of the electrode decreased to a level that is commensurate with the hole diffusion length.[22,23] Optimized thin films deposited by atmospheric pressure chemical vapor deposition (APCVD) have a dendritic structure with branches 10−20 nm. These films showed photocurrents of 2.3 mA cm^{-2} at 1.23 V vs RHE under 1 sun illumination (AM 1.5 global, 1000 W m^{-2}) with the aid of a cobalt catalyst, and 1.8 mA cm^{-2} in the absence of the surface catalyst.[24] Besides the effect of the feature size, the addition of silicon as an n-type dopant and the deposition of a silicon oxide underlayer were crucial for obtaining an electrode photo activity that exceeded that of single crystals of hematite.[6]

While this latest benchmark for solar water splitting with hematite has sparked new interest in this system within both industrial and academic arenas, the full potential of hematite has yet to be realized; the maximum quantum efficiency is only one-half that of other rigorously optimized materials like TiO$_2$ and WO$_3$.[10,25] To more fully understand the extraordinary performance of the APCVD hematite films and to precisely define the remaining limitations of this system, we present here a detailed investigation of the system's most important parameters. The central roles of the dopant, feature size, and film thickness are examined in the context of solar photocurrent, quantum efficiency, and material properties. In addition, a correlation between feature size and Raman spectra is presented and discussed in the context of disorder in the crystal structure. Finally, impedance spectroscopy provides evidence of an unusually high donor density in the silicon-doped photoanodes,

which would allow a space-charge layer to be formed inside the nanosized features of the polycrystalline film.

2. Experimental Section

Mesoporous films of hematite were grown on transparent conductive substrates (SnO$_2$:F, TEC 15, Hartford Glass Co. 15 $\Omega/\square$, 50 × 13 × 2.3 mm^3) from the atmospheric pressure chemical vapor deposition of the precursors, Fe(CO)$_5$ and tetraethoxysilane (TEOS). A full description of the deposition method is found elsewhere.[24] The films were deposited at substrate-heater temperatures between 450 and 490 °C to find the optimum deposition temperature. The actual temperature of the SnO$_2$ surface was 35 °C lower due to the gas stream and the lower surrounding room temperature. To study the influence of film thickness on the front and back side photoresponse, films were deposited with deposition times between 48 s and 10 min. On each substrate, two circular spots of 1 cm in diameter were deposited sequentially 3 cm apart. In contrast to the previous work, the films received no catalytic coating with Co(NO$_3$)$_2$.

Photocurrent measurements were performed to determine the solar to hydrogen energy conversion efficiency in a three electrode configuration with 1 M NaOH (pH = 13.6)[7] as electrolyte using Ag/AgCl in saturated KCl as a reference electrode. The hematite electrode was scanned at 50 mV s^{-1} between −300 and 800 mV vs Ag/AgCl. The potential is reported relative to the reversible hydrogen electrode potential (RHE) at the pH of the electrolyte.[24] The photocurrent is reported at 1430 mV vs RHE as most current−voltage curves show a photocurrent plateau around this potential. The samples were illuminated with simulated sunlight from a 450 W xenon lamp (Osram, ozone free) using a KG3 filter (3 mm, Schott). Photocurrent action spectra are measured to determine the incident photon to current conversion efficiency (IPCE) and to study the influence of the light penetration depth on the photoresponse. These spectra were obtained under light from a 300 W Xe-lamp with integrated parabolic reflector (Cermax PE 300 BUV) passing through a monochromator (Bausch & Lomb, bandwidth 10 nm fwhm). References made to front side and back side illumination are defined as illumination through the electrolyte/hematite and substrate/hematite interface, respectively. A detailed description of the setup and determination of the IPCE is found elsewhere.[24] Electrochemical impedance spectroscopy measurements to estimate the donor density and the flat-band potential of the films were performed using the same three-electrode configuration with the exception that the electrode was pressed onto an aperture sealed with an O-ring (i.d. 6 mm) on the back of the cell to obtain a defined geometric surface area of 0.283 cm^2. Spectral mismatch factors to estimate the difference of the electrode photoresponse obtained from simulated sunlight and real sunlight at AM 1.5 G[26] were calculated according to the method described by Seaman et al.[27]

The absorption of the mesoscopic hematite layers in the UV−vis range was determined by wetting the films with electrolyte solution and covering them by a quartz window to determine the light absorption depth and the internal quantum yield, referred to as absorbed photon to current conversion efficiency (APCE). The absorption spectrum was measured against the uncoated substrate as a blank without further corrections for reflection and scatter losses from the Fe$_2$O$_3$ layer.

As the size of electrode's surface features is thought to influence the photoresponse of the photoelectrodes, the surface morphology and cross-section of hematite films on the conducting substrate were investigated with a high-resolution scanning electron microscope equipped with a field emission gun (Philips
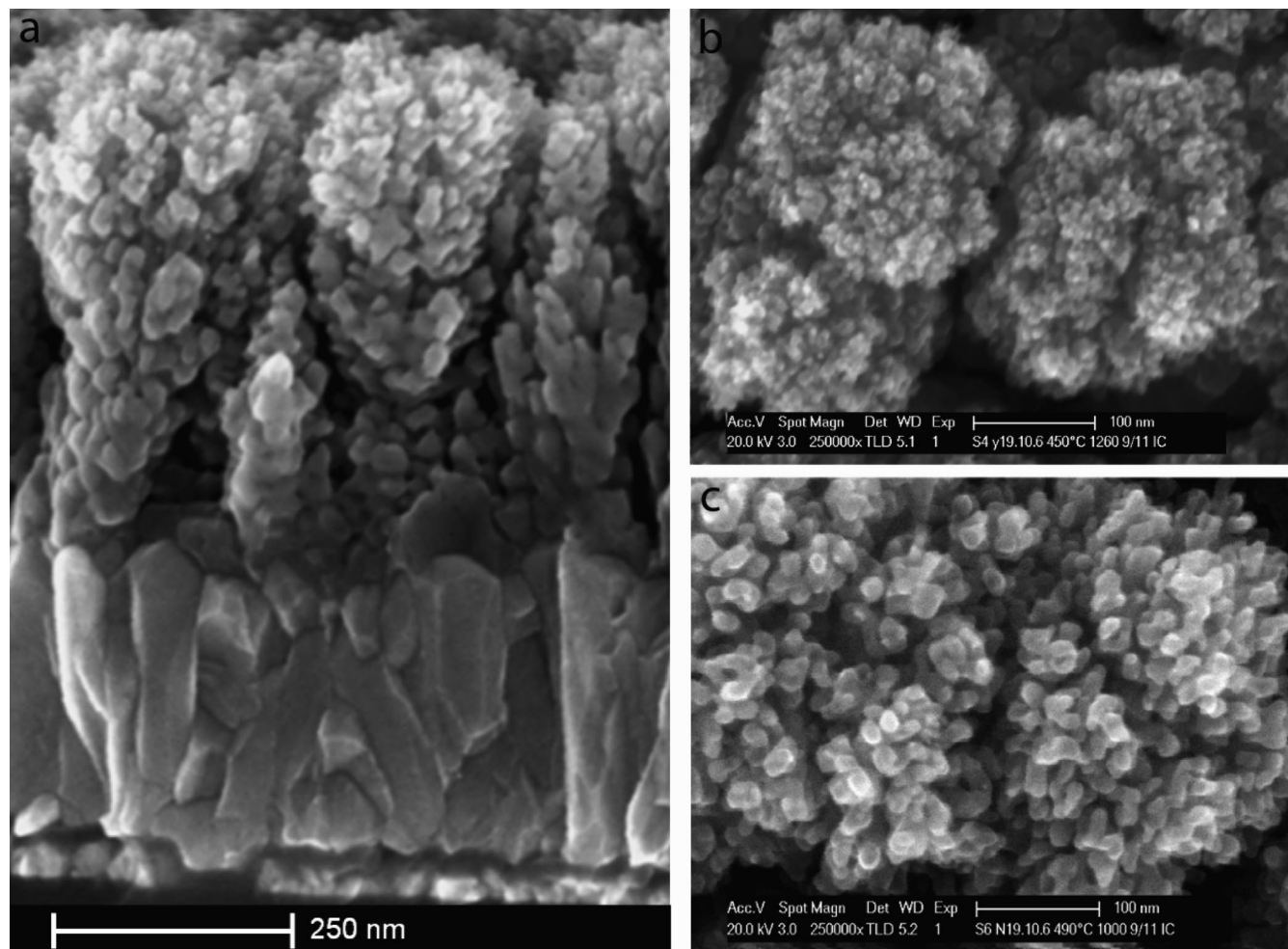
Figure 1. HR-SEM images of the morphology of mesoporous Si-doped hematite films, prepared at two different deposition temperatures, 450 °C (a and b) and 490 °C (c). A cross-sectional view is shown in (a), while (b) and (c) show top-down views.

XL-SFEG) to resolve to a feature size down to 4 nm. The images were taken with an acceleration voltage of 5 keV and a 5 mm working distance using an in-lens detector.

To determine the crystalline quality of the deposited hematite films, Raman and Mössbauer experiments were performed. Raman spectra were obtained using a Renishaw 2000 Micron Raman setup with a 514.5 nm line from an argon ion laser. The incident power was kept below 0.7 mW with a spot size of 25 μm to prevent in situ phase transformation from other phases into hematite induced by local laser heating.[28] The spectra were obtained between 197 and 1633 cm^{-1} with a resolution of 2.5 cm^{-1}. The integration time was 1 min for each spectrum. To compare these results with pure Fe_2O_3 samples, a calibration series was prepared. A series of hematite (Aldrich 99.98%) and magnetite (99.99%) powders were mixed with content between 0 and 50% in weight, pressed into pellets, and analyzed in the same manner. To relate the Raman 660 cm^{-1} peak area to the weight fraction of magnetite, a linear relation was obtained (N = 5, R^2 = 0.97) for the 660/610 cm^{-1} peak area as a function of the magnetite content in wt % with a slope of 5.1 [ratio peak area/magnetite content in %] and an intercept of 0.26 [ratio peak area].

Room-temperature conversion electron Mössbauer spectra (CEMS) were recorded in a constant acceleration mode using a ^{57}Co radioactive source and a proportional continuous gas flow detector (90% He + 10% CH_4). Spectra were registered in 1024 channels.

To measure the space-charge capacitance in our films, the ac-impedance was measured with a sinusoidal voltage perturbation of 20 mV amplitude superimposed on a bias voltage with a frequency that ranged from 100 kHz to 1 Hz. The bias potential was scanned cathodically from 1.6 to 0.4 V vs RHE with a 50 mV interval.

3. Results and Discussion

3.1. Growth Temperature and Feature Size. Representative HR-SEM images of the as-deposited hematite are presented in Figure 1. A cross-sectional view (Figure 1a) shows that typical cauliflower type aggregates (100−200 nm range) obtained by the APCVD technique[24] are composed of large aggregates at the base, which become progressively smaller near the top. The substrate temperature was found to have a large influence on the size of the topmost features. This is clearly seen in Figure 1b and c and summarized in Table 1. The average primary surface particle size increased from 6 to 17 nm between 450 and 490 °C.

Growth Mechanism. In addition to the changing feature size, we observed a slower growth rate of films at higher temperature for the range tested (not shown), and in general a low deposition efficiency (i.e., only about 1% of the iron precursor deposits on the substrate). On the basis of these observations, a likely growth mechanism can be proposed. As the reported half-life for $Fe(CO)_5$ is 5.3 ms at 300 °C,[29] it is expected that the bulk of the precursor is oxidized to iron oxide in the gas phase above

Nanostructured Hematite Photoanodes

J. Phys. Chem. C, Vol. 113, No. 2, 2009 **775**

TABLE 1: Average Feature Size and Standard Deviation of the Top Layer Morphology Together with Raman Peak Area Ratio 660/610 cm^{-1} of Iron Oxide Films Prepared at Various Substrate Temperatures with and without Silicon Doping

	450 °C Si doped	470 °C Si doped	490 °C Si doped	470 °C undoped
average feature size [nm]	6.1	11.8	17.0	25.0
standard deviation [nm]	1.6	2.2	3.9	6.3
ratio peak area 660/610 cm^{-1}	2.2	1.2	0.8	0.3

the substrate via homogeneous nucleation. This hypothesis is supported by the report of Orthner et al., who prepared iron oxide nanoparticles through homogeneous nucleation under similar conditions.[29] As such, our hot substrate is subjected to an aerosol consisting of nanoparticles plus residual precursor gas both at different concentrations depending on substrate temperature. Further, it is well-known that particles exposed to a temperature gradient are repelled from a hot surface.[30,31] Because this thermophoretic force increases with particle size, only the smallest particles are expected to reach the surface and attach to the growing film. Simultaneously, the residual precursor concentration would enable further crystal growth. In this circumstance, one would expect the ratio of these gaseous precursors to nanoparticles to increase with temperature, and thus there would be an increase in feature size with temperature. In addition, as the film thickens with time during the deposition, the precursor concentration in the pores of the film decreases as it is progressively consumed by crystal growth at the top of the film. This limits the growth of the features at the bottom and explains the observed residual porosity there. Alternatively, the feature size and the porosity near the bottom of the film can be explained by the sintering of smaller particles in the complete absence of residual precursors. Both explanations are consistent with the cessation of pore filling near the substrate at a particular film thickness. From the cross-sectional SEM,[24] this threshold film thickness can be estimated to be 250−300 nm. Finally, the preferential orientation reported for these films[24] can be the result of rotation of newly attached primary particles followed by preferential attachment. This coalescence occurs preferentially between particles of similar crystallographic orientation as proposed by Ribeiro et al.[19]

Photoresponse. The important performance metric of water splitting photoanodes is the stable photocurrent directly corresponding to oxygen evolution. Figure 2 shows the influence of the deposition temperature on the solar (AM 1.5 G, 100 mW cm^{-2}) photocurrent behavior of the hematite electrodes presented in Figure 1 and Table 1, illuminated from the front side. The photocurrent shows a maximum of 2.3 mA cm^{-2} at 1430 mV vs RHE for the 470 °C deposition temperature. The photocurrent maximum observed for samples prepared at 470 °C can be interpreted in terms of the intrinsic hole diffusion length, feature size, and charge transport. Classically, charge transport occurs via two mechanisms: a space-charge electric field and the diffusion driven by concentration gradients. Understanding the relative influences of each mechanism is an important task and will be discussed later. However, Kennedy et al.[4] reported the average hole diffusion length before recombination to be 2−4 nm for sintered pellets of silicon-doped hematite electrodes. Accordingly, a feature size below 10 nm would ensure that the majority of holes reach the surface to participate in water oxidation even in the absence of a space-charge electric field. This size matches nicely with the average feature size of 11.8 nm obtained at 470 °C and even exceeds the 6.1 nm obtained at 450 °C. For holes that are generated appreciably more than 5 nm from the semiconductor/electrolyte interface, the path length to the surface rises beyond their diffusion length, thus increasing their probability to recombine with electrons. Ac-
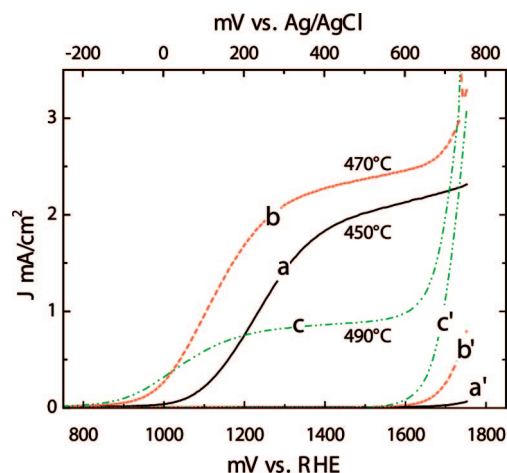

Figure 2. Current density plots (reported relative to the reversible hydrogen electrode, RHE) of mesoporous silicon-doped hematite photoanodes prepared at various deposition temperatures (indicated next to curve) measured in 1 M NaOH (pH 13.6), at 50 mV s^{-1}, in dark (a′, b′, c′) and under illumination (a, b, c) of simulated sunlight (AM 1.5 G, 100 mW cm^{-2}).

cordingly, the dramatic decrease in photoresponse at 490 °C coincides with a significant increase in feature size to 17 nm. In addition to absolute photocurrent, a 200 mV cathodic shift of the photocurrent onset is observed as the temperature increases from 450 to 470 or 490 °C. This shift can also be explained in terms of feature size when also considering the surface recombination rate. Assuming that the surface state density and type is not significantly affected by the higher deposition temperature ($\Delta T = 40$ °C), a lower semiconductor surface area could account for a lower recombination rate. The reduced recombination rate would allow for a higher electron density buildup and thus a more anodic photocurrent onset. Interestingly, the photocurrent plateau and onset as well as the transient onset potential of silicon-doped film prepared at 490 °C resemble that of hematite electrodes deposited by ultrasonic spray pyrolysis with perpendicularly oriented leaves of similar feature size.[23]

Raman, Mössbauer, and Lattice Disorder. In many other iron oxide deposition techniques, crystal phases other than hematite have been observed, and their presence can drastically affect photoanode performance.[32] To further characterize the hematite thin films from APCVD, the temperature series samples along with an undoped iron oxide film (deposited at 470 °C) were analyzed by Raman microspectroscopy and conversion electron Mössbauer spectroscopy (CEMS). The micro-Raman results (Figure 3) show the typical bands of hematite, A$_{1g}$ (222, 496 cm^{-1}), E$_g$ (242, 291, 408, 610 cm^{-1}), and 2-magnon scattering (1313 cm^{-1}) bands, are observed with a small contribution from the substrate between 1050 and 1150 cm^{-1}. The series shows a remarkable development of the 660 cm^{-1} band with decreasing feature size of the top layer as reported in Table 1. The area ratio of the 660 and 610 cm^{-1} peaks increases approximately linearly from 0.3 to 2.2 as the average feature size decreases from 25 to 6.1 nm. We note that all E$_g$ bands and the 2-magnon scattering band increase in intensity
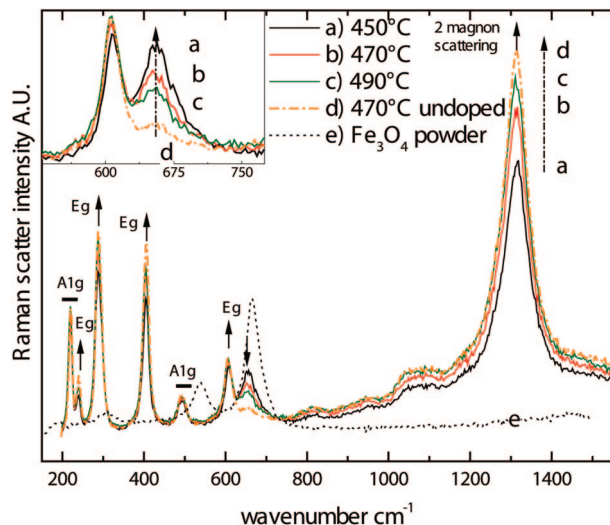
Figure 3. Micro-Raman spectra of mesoporous iron oxide films on conducting transparent substrates deposited at different substrate temperatures with and without silicon doping as compared to commercial Magnetite powder. Traces are labeled a−e according to the legend, and arrows indicate whether the peak area increases (↑), decreases (↓), or remains constant (−) as the particle size increases (λ = 514.5 nm, power < 0.7 mW, spot size = 25 μm, integration time = 1 min). The inset shows a magnification of the region from 525 to 775 cm^{-1}.

as the 660 cm^{-1} peak intensity decreases, while the A_{1g} bands remain unchanged. All peak positions are constant, and three of the eight hematite bands show an increase in HWHM as the 660 cm^{-1} peak intensity increases (291, 408, and 496 cm^{-1}). Because magnetite (Fe_3O_4) has a strong Raman band at 660 cm^{-1}, it seemed possible that small magnetite inclusions in the film are responsible for this peak. By comparing the 660/610 cm^{-1} peak area ratio to the calibration curve compiled from pure hematite and magnetite samples, the amount of magnetite that would result in the observed intensity of the 660 cm^{-1} band was estimated to be 18 wt % for the best performing sample (prepared at 470 °C).

However, the data from the CEMS (Figure 4) show no indications of the presence of other iron oxides (magnetite, maghemite, β-, ε-Fe_2O_3) within the 3% detection limit of the method.[33] Figure 4 clearly illustrates only the magnetically split component (sextet) with the hyperfine parameters corresponding well to α-Fe_2O_3 (hematite). This, with the addition of previously presented XRD results,[24] strongly indicates that magnetite impurities are not responsible for the 660 cm^{-1} Raman peak, as has been frequently suggested in literature.[23,32,34] Similar Raman peak results are reported for powders by Bersani et al.[28] These authors attributed the 660 cm^{-1} peak to "the disorder-induced activation of the IR-mode present at the same wavenumber", as has also been found for Fe_2O_3:Cr_2O_3 mixtures.[35] Such a disorder could be induced by substitution of iron by dopant elements or by the small grain size, which increases the relative amount of surface atoms with different coordination spheres. This is consistent with the fact that the 660 cm^{-1} peak intensity rises upon the addition of silicon, as well as with decreasing feature size. Finally, the strong correlation of the peak intensity with feature size at constant TEOS concentration demonstrates that the feature size alone has a significant influence on this observed disorder. In general, it can be said that the particle size and crystal order increase with deposition temperature. As the particle size increases, the surface recombination rate is probably reduced by a lower surface area and a lower trap density as the crystal order increases. Both of these

factors likely contribute to the anodic shift of the photocurrent onset potential. In addition, from these observations, it becomes clear that feature size and the surface recombination (driven by area and disorder) must be balanced to obtain optimal saturation photocurrent.

3.2. Film Thickness and SnO_2−Fe_2O_3 Interface. Because hematite is an indirect band gap semiconductor with a relatively large absorption depth, constraints are not only posed on the feature size of the ideal photoanode, but also on the film thickness. Next, the photoelectrochemical performance of photoanodes with different thicknesses is analyzed and discussed in the context of the quantum efficiency. This allows us to more precisely identify the limitations of the APCVD films.

Film Thickness Determination. To further characterize the hematite photoanodes with varying thickness, the light penetration depth and film thickness were estimated from the optical transmittance, T, as a function of the deposition time, t, assuming a Lambertian absorption with an absorption coefficient, α, and a lag time for nucleation followed by linear growth at rate k_{growth} (no correction was made for porosity, reflection, or scatter losses):

$$-\ln(T) = \alpha \cdot k_{growth} \cdot (t - t_0) \qquad (1)$$

A layer thickness of 415 nm after 300 s was determined from HR-SEM images of a film cross-section. The model proves adequate as illustrated by Figure 5, yielding an incubation time of 17 s and a growth rate of 1.5 nm s^{-1}. The light penetration depth is defined as α^{-1} and corresponds to the length over which 63% of the photons are absorbed. Values for α, obtained from eq 1 and the known thickness after 300 s, were calculated for different wavelengths and are summarized in the inset of Figure 5. The penetration depth ranges between 46 and 118 nm for the wavelengths of 450 and 550 nm, respectively, and agrees reasonably well with a similar report with rough thin films of hematite prepared by radio frequency sputtering.[36] The calculated film thickness after 48 s, 1, and 3 min is 45, 63, and 239 nm, respectively. On the basis of the growth rate of 1.5 nm s^{-1}, a deposition area of about 1 cm^2, the density of hematite of 5.28 g cm^{-3} (neglecting the porosity of the film), and the mass flow rate of 3.5 mg min^{-1} of iron pentacarbonyl, a deposition efficiency in the order of 1% is obtained for films grown at 470 °C, and decreased for increasing temperature presumably due to material loss from the thermophoretic effect.

Solar Photo Response. The current−voltage curves for the layer thickness series are illustrated in Figure 6. The front side photocurrent plateau at 1430 mV vs RHE increases from 1.1 to 2.0 mA cm^{-2} between 48 s and 3 min of deposition, whereas it remains nearly constant between 3 and 5 min. At longer deposition times, the reproducibility of the photoresponse decreased, but in general, films deposited for 7 min (not shown) performed similarly to samples deposited for 5 min. However, after 10 min of deposition, the photocurrent plateau collapses to less than 1 mA cm^{-2} (not shown). In contrast to the frontside photocurrent data, a much lower photoresponse is observed under illumination from the backside. The back side photocurrent plateau increases between 48 s and 1 min from 0.86 to 1.1 mA cm^{-2} at 1430 mV vs RHE. Remarkably, this latter value is maintained for deposition times up to 10 min. With this observation, two conclusions can be made. (1) Although the stems widen during the deposition, the film maintains a degree of porosity that assures the intimate contact between hematite and electrolyte near the substrate. This is in agreement with the porosity observed in HR-SEM images of the film cross-section (Figure 1a). (2) The mass transport of oxygen from the bottom of the stems across a film thickness of 875 nm does not
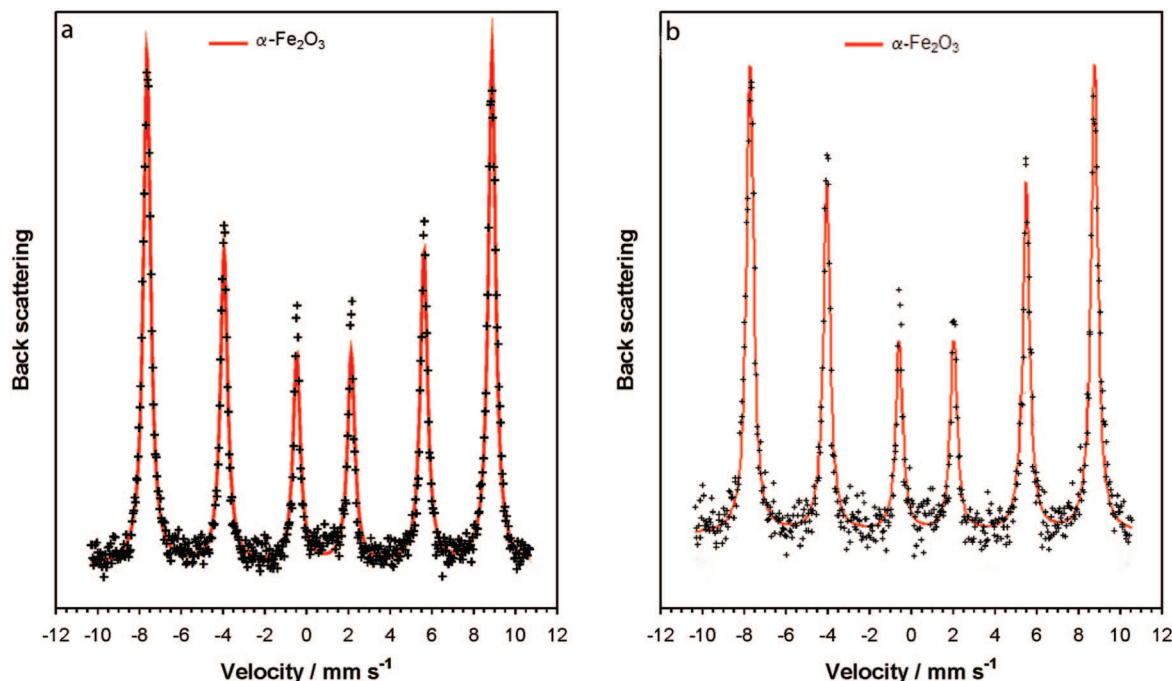
Nanostructured Hematite Photoanodes

J. Phys. Chem. C, Vol. 113, No. 2, 2009 **777**

Figure 4. Conversion electron Mössbauer spectra of mesoporous iron oxide films on conducting transparent substrates deposited with (a) and without (b) silicon doping. The expected trace for α-Fe_2O_3 is shown superimposed on the data points.
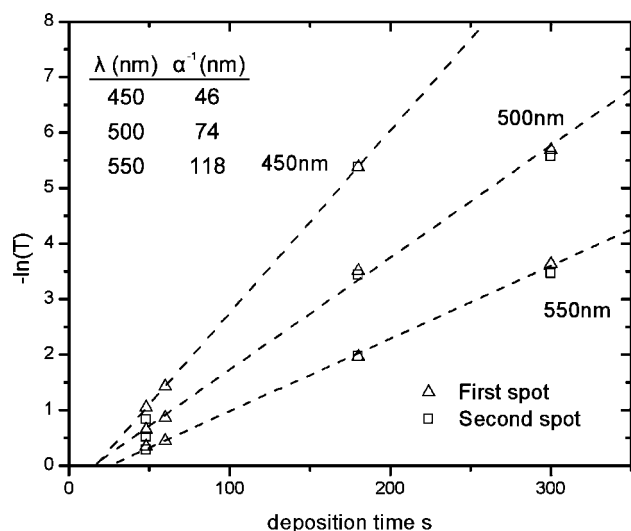

Figure 5. Film growth characteristics illustrated in terms of the negative natural logarithm of the transmittance vs deposition time at λ = 450, 500, and 550 nm. Duplicate data points for the first and second deposition spot show the reproducibility, and the inset table reports the calculated penetration depth (α^{-1}, see text) for the indicated wavelengths.

Figure 6. Current density plots (reported relative to the reversible hydrogen electrode, RHE) of mesoporous silicon-doped and undoped hematite photoanodes prepared at deposition times between 48 s and 10 min, measured in 1 M NaOH (pH 13.6), at 50 mV s^{-1}, under illumination with simulated sunlight (AM 1.5 G, 100 mW cm^{-2}). Each curve is labeled with the corresponding deposition time (1' = 1 min), and the solid and interrupted lines correspond to illumination through the front and back side (bc), respectively, with the front side being defined as the electrolyte/semiconductor interface. The additional curve label "no Si" indicates undoped films.

limit the photocurrent. A similar reasoning can be applied for the saturation of the front side photocurrent plateau. Here, most electrons are photogenerated over an equal distance (200 nm) in the topmost layer of the film. As the photocurrent plateau remains constant up to a film thickness of 605 nm (7 min deposition), it can be concluded that no electron transport limitation occurs over a distance of 605 nm in the case of a silicon-doped film. The omission of TEOS during film growth, however, causes a drastic decrease of performance. As the feature size of undoped samples (25 nm, Table 1) is 5 times the hole diffusion length, it is not surprising that the observed photocurrents are 3 times lower than those for doped samples (feature size 12 nm). In addition, the absence of dopant alters the donor density and accordingly changes the space-charge
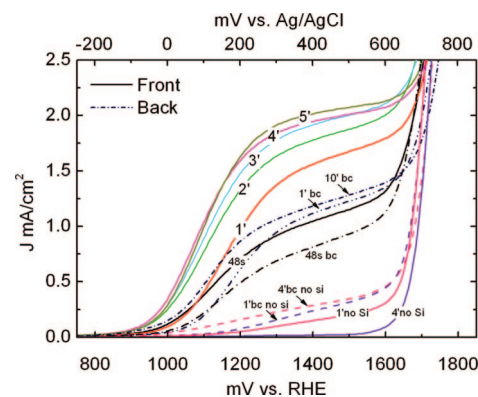
electric field (see later discussion on doping and charge separation). These undoped films also show an electron transport limitation at a significantly shorter distance than the doped films. This is clear by comparing the front and back side photocurrents. For deposition times of 1 and 4 min, the front side photocurrent at 1.43 V vs RHE drops from 170 to 20 μA cm^{-2}, while the back side photoresponse rises moderately from 260 to 310 μA cm^{-2}. The front side photocurrent becomes negligible at a film thickness between 65 and 330 nm (1 and 4 min deposition, Figure 6). Interestingly, the back side photocurrent exceeds that of the front side over the complete voltage range for both film thicknesses, and the difference between the front and back side photocurrent becomes larger as the film thickens. This suggests that the electron transport from the top of the film depends strongly on silicon doping. Similar trends have been observed
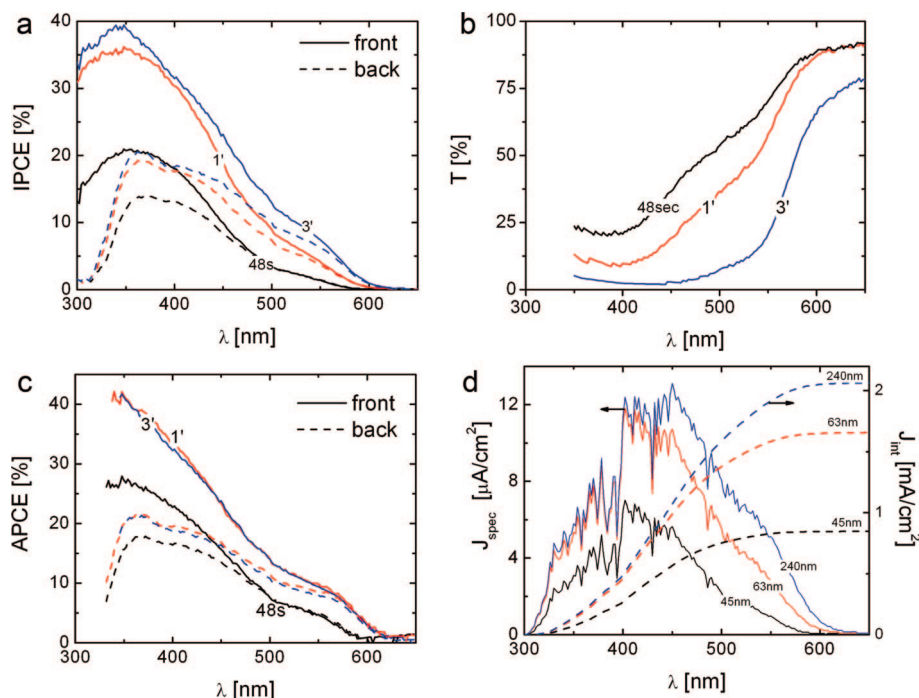
Figure 7. Spectral response of mesoporous silicon-doped hematite films on conductive SnO$_2$:F deposited for 48 s, 1, and 3 min. (a) Incident photon to current conversion efficiency, (b) transmittance vs substrate as blank, (c) absorbed photon to current efficiency (quantum yield), and (d) solar photocurrent spectra (J_{spec}) and integrated solar photocurrent (J_{int} at AM 1.5 G, 100 mW cm^{-2}).

for silicon-doped hematite electrodes prepared by ultrasonic spray pyrolysis.[37] These observations reinforce the assumption that the main role of the TEOS dopant is not solely to affect the feature size, but to enhance the conductivity by acting as an electron donating dopant.

Photocurrent Action Spectra. The incident photon to current efficiencies (IPCE) measured at 1.43 V vs RHE are presented in Figure 7a. All samples show a maximum IPCE between 350 and 370 nm, while the photoresponse drops gradually at longer wavelengths and drops to zero at 610 nm (2.0 eV). The front and back side illumination IPCE for longer wavelengths (400−610 nm) rises monotonically with deposition time from 48 s to 3 min. At 550 nm, the front side illumination IPCE increases from 2% to 9% for deposition times of 48 s and 3 min. At 350 nm, it saturates between 35% and 40% after 60 s of deposition. The back side illumination IPCE shows a sharp decrease below 350 nm due to the absorption of the glass substrate. The optical transmittance of these films is presented in Figure 7b and shows a decrease in transmittance with larger film thickness. For films deposited during 48 s and 3 min, the transmittance at a wavelength of 400 nm decreases from 20% to 2.4% and for 550 nm from 70% to 21%. Combining the IPCE and the transmission data allows us to calculate the absorbed photon to current efficiency (APCE, quantum yield). A strong drop in APCE with increasing wavelength is observed for all samples independent of deposition time (Figure 7c). For samples deposited between 1 and 3 min, the APCE spectra overlap in the entire spectral range (320−610 nm) and decrease from 40% at 350 nm to 10% at 550 nm when illuminated from the front side. This overlap is consistent with the fact that at these film thicknesses photons are absorbed in a film that mainly consists of fine branches with feature sizes comparable to the hole diffusion length. This appears to be the case as the film thicknesses range between 68 and 240 nm, while a significant coarsening of the stems appears only above a film thickness of 200−250 nm (Figure 1a). Photons that show the largest quantum yield (λ < 400 nm) are absorbed in the top 50 nm, and as the

feature size is independent of deposition time, the quantum yield remains constant. The same trend, although less pronounced, is observed for back side illumination with APCE values of 20−22% and 8−9% for 350 and 550 nm, respectively. As the film becomes more transparent at longer wavelengths (the penetration depth increases), the number of photons absorbed at both sides of the hematite film becomes similar and thus increasingly independent of illumination direction. This is the reason why the APCE spectra for both illumination directions approach each other at longer wavelengths. This overlap occurs as the penetration depth becomes significantly larger (∼2 times) than the film thickness. For the thinnest film deposited for 48 s (thickness = 45 nm), this spectral overlap occurs before 500 nm (α^{-1} = 78nm), while for thicker films (86 and 240 nm), the overlap occurs near the band gap at around 600 nm.

Finally, the solar photocurrent spectra, obtained by multiplication of the IPCE with the photon flux density of global sunlight (1 kW m^{-2} AM 1.5 Global) as well as the integrated solar photocurrent, are presented in Figure 7d. As expected from the IPCE measurements, the increase in solar photocurrent between 48 s and 1 min originates from an increased photocurrent generation over the entire spectral range. By contrast, the increase in photocurrent between 1 and 3 min originates from the enhanced contribution of longer wavelengths between 450 and 610 nm. The integrated solar photocurrent values at 1.43 V vs RHE are 0.85, 1.66, and 2.06 mA cm^{-2} for 48 s, 1, and 3 min. These values deviate from the white light photocurrents presented in Figure 6 by less than 10% for films deposited between 1 and 3 min. The sample deposited for 48 s deviates by 20%.

SnO$_2$/Fe$_2$O$_3$ Interface. A closer look at the photoelectrochemical performance of this thickness series allows us to make some observations about the semiconductor/TCO interface. Strikingly, much lower APCE values (nearly 2 times smaller) are obtained over the entire spectrum and regardless of illumination direction for the thinnest sample deposited (48 s deposition with values of 26% and 3% for 350 and 550 nm for front side

Nanostructured Hematite Photoanodes

J. Phys. Chem. C, Vol. 113, No. 2, 2009 **779**

illumination), as compared to the thicker samples (1 and 3 min). The poor photoresponse of this thin film can be ascribed to an increased recombination rate compared to thicker films. This poor performance cannot be attributed to a mismatch between feature size and hole diffusion length as the top morphology and feature size are independent of deposition time. Nor does its Raman spectrum (not shown) contain any anomalies other than enhanced intensities of substrate bands. This exact same trend was observed for samples prepared by spray pyrolysis by Itoh et al.,[16] as well as ultrasonic spray pyrolysis.[37] Itoh et al. reported negligible photocurrents for films below 20 nm and suggested that the electron cloud of the fluorine-doped SnO_2 extends into the Fe_2O_3 film and thus enhances recombination. Alternatively, recombination sites at the SnO_2/Fe_2O_3 interface could play a role in the recombination mechanism in analogy to surface recombination found at the Fe_2O_3/electrolyte interface.[38–41] This could be related to diffusion of fluorine from the substrate or crystalline defects at the interface. If the enhanced recombination rate at the SnO_2/Fe_2O_3 interface is an intrinsic property of this system, there would be far-reaching consequences for the prospects of using these materials for efficient nanoporous core—shell electrodes in a host/guest approach.[37,42] Here, thin hematite coatings with thicknesses that approach the hole diffusion length are envisaged to be conformally coated on nanoporous SnO_2 with a large specific surface area that serves as an efficient electron collector. As in this configuration all electron—hole pairs are generated in the vicinity of the SnO_2/Fe_2O_3 interface and thus rapidly recombine, it is not likely that this core—shell approach will yield high photo conversion efficiencies without first addressing this problem. In fact, examples of these composite electrodes, based on tin oxide nanospheres or arrays of nanorods perpendicular oriented to the substrate, were successfully prepared and characterized in our laboratory but yielded no significant photocurrents.[37]

Wavelength Dependency Quantum Yield. For hematite, it is important to understand the relation between quantum yield and photon energy because 50% of solar energy available to hematite lies in the wavelength range between 510 and 610 nm. Our detailed APCE analysis here shows very poor quantum efficiency in this range. However, it is unlikely that the feature size is the sole reason for this poor performance as we suggested earlier.[24] If the quantum yield is only dependent on the feature size, then the APCE spectra should become less dependent on the wavelength for films that mainly consist of the fine-structured top layer (63–240 nm) as all photons are absorbed by crystals of similar size. However, the wavelength dependency is still maintained (Figure 7c), which suggests reasons other than feature size are important. It has been proposed that this wavelength dependence is due to the stronger oxidizing power of holes generated in the valence band at oxygen sites by a direct transition below 400 nm (O^{2-} $2p^6 \rightarrow Fe^{3+}$ 3d) as compared to holes generated by iron sites alone due to an indirect transition between 400 and 620 nm (Fe^{3+} 3d $\rightarrow$ 3d).[7,43] This could explain the wavelength dependency of the quantum yield in our films if these "hot carrier" holes were diffusing to the interface and participating in water oxidation before thermalizing to the lower energy state. However, this purported mechanism becomes questionable as we notice no abrupt change in the quantum efficiency near the direct-indirect transition. Ultimately, a better understanding of the interfaces, charge transport, carrier lifetimes, and the water oxidation reactions is needed to fully elucidate this issue.

3.3. Impedance Spectroscopy. With the aim of completing the understanding of charge transport in the hematite APCVD

photoanodes, the complex impedance of the mesoporous thin films was measured to establish the donor density and the flat band potential. If the previously reported 1.6 atom % of silicon content in the film corresponds directly to the effective donor density, an interesting behavior of the electrode's capacitance is expected. The space-charge layer would be thin enough to fit inside individual nanocrystals and affect the transport of holes to the surface during illumination. A comparative study was performed on an undoped and a silicon-doped film deposited for 5 min at 470 °C. A Mott—Schottky analysis is used on the experimental capacitance data as a function of potential to obtain the donor density and the flat band potential from the slope and intercept, respectively, from data plotted on C^{-2} versus V plots. This Mott—Schottky analysis is based on a few assumptions. First, the positively charged electron donor ions need to be immobile, fully ionized, and homogeneously distributed throughout the width of the space-charge layer. Second, the surface should be flat to approximate a parallel plate capacitor.[11] It is obvious from the morphological study that the flat surface condition is not met. However, if the width of the space-charge layer is small as compared to the radius of the semiconductor surface curvature, it is possible to approach the flat surface condition. This has been first demonstrated by Boschloo et al.[44] in nanoporous antimony-doped tin oxide of similar feature size ($\sim$5 nm in diameter) with an estimated donor density of 3 × 10^{20} cm^{-3}. With a donor density in the same order of magnitude in hematite and a dielectric constant of 80,[7,45] the space-charge layer would range between 3 and 9 nm for a Schottky barrier (V_s) between 0.1 and 1 V. On the basis of this space-charge layer width, it is assumed that the flat surface condition is approached for small values of V_s of around 0.1 V. A quantitative estimation of the error that can be expected was reported by Mora-Sero et al.[46] These authors have studied the complex impedance of nanosized ZnO cylinders, on average 93 nm in diameter and 830 nm in length, that were perpendicularly oriented on a F:SnO_2/glass substrate and derived the Mott—Schottky relation for a cylindrical geometry. They demonstrated that a very high donor density of 10^{20} cm^{-3} would result in a linear Mott—Schottky plot. A fit with a Mott—Schottky relation for a flat surface underestimated the donor density by 20%. It was shown that a decrease in donor density by 2 orders of magnitude resulted in a super linear curve due to the increased space-charge layer width, becoming commensurate with the mesoscopic feature size of the electrode. Similar findings are presented in this work.

Donor Density of Silicon-Doped Films. The complex component of the impedance data acquired as described in the Experimental Section was used to calculate the overall circuit capacitance, and the capacitance of the space-charge layer was extracted from these data using three circuit models of increasing sophistication to determine the dependence of the values for the donor density and flat band potential on the equivalent circuit used to fit the data. First, a simple series RC circuit (Figure 8, inset model a) was used to fit the circuit capacitance in the frequency range between 222 and 1456 Hz, where the slope of the imaginary impedance as a function of frequency was close to −1 and the real part was not a function of the frequency. At frequencies lower than 222 Hz, the real part increased, while at frequencies higher than 1456 Hz, the slope deviated more strongly from −1 and had a poor signal-to-noise ratio. The fitted resistance (real part of the impedance) ranged from 63.0 to 64.0 Ω, and the slope of the imaginary part ranged from −0.89 to 0.94 for a voltage range of 0.5–1.5 V vs RHE. The fitted capacitances that range from 18 to 80 μF between 1.6 and 0.4
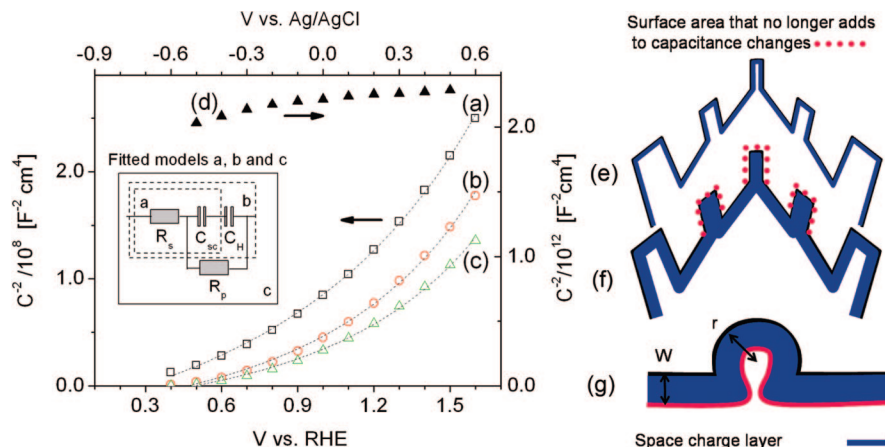
Figure 8. Mott–Schottky plots of Si-doped (curves a–c) and undoped (curve d) mesoporous hematite photoanode. The capacitances for curves a, b, and c are obtained from the silicon-doped sample and models a, b, and c, respectively, shown in the inset of the left-hand plot. Curve d is obtained from the undoped film and model a (series RC). The dashed lines connecting the data points represent the variable active surface area fit (see text). Sketches e–g depict the development of the space-charge layer in a mesoporous semiconductor as function of applied potential, illustrating a decrease in active surface area at advancing space-charge layer width in two dimensions. (e) Near flat band potential with maximum surface area. (f) Total depletion of smaller feature at increased bias potential. (g) Decreased active surface area in concave curved surface.

V vs RHE were used to plot C_{sc}^{-2} versus V (Mott–Schottky plot, Figure 8, curve a). A super linear curve is obtained with an intercept near 0.3 V vs RHE. Earlier, we reported a surface roughness for these electrodes of around 20 calculated from the surface adsorption of the orange II dye.[24] Based on this value, the total semiconductor surface that is in contact with the electrolyte would be 5.7 cm^2, which corresponds to a maximum space-charge capacitance of 14 μF cm^{-2}. This value is close to the widely reported Helmholz capacitance, C_h, of 20 μF cm^{-2}.[45,47] Because the observed capacitance is actually a reciprocal sum of C_h and C_{sc} (as they are in series), a more accurate determination of the actual C_{sc} (and thus flat band potential and donor density) can be found using a new circuit model (Figure 8a, model b) by adding an additional capacitor (in series with model a) to represent the Helmholz capacitance of the total wetted electrode surface (20 μF cm^{-2} × 5.7 cm^2 = 114 μF). Model b was fit in the same frequency range, and the obtained capacitances form a similarly shaped curve to model a however shifted 200 mV anodically. This is expected as C_h should not be a function of potential and should only act on the flat band potential as discussed by de Gryse et al.[48] One further refinement of the circuit model allowed the data to be fit over the complete frequency range: a resistor element was added in parallel to both capacitors to account for charge-transfer across the electrode/electrolyte interface (model c). The addition of the parallel resistor does not change the Mott–Schottky plot much. The error of all fitted elements was lower than 5% in all cases.

The slope and intercepts used to determine the donor density and flat band potential of the hematite film, respectively, were determined with a linear fit in the potential range between 0.4 and 0.55 V vs RHE for circuit models b and c. In this range, close to the flat band potential, the space-charge layer is thin and the Mott–Schottky assumption of a flat electrode surface is best approximated. The intercepts for model b and c are 0.38 and 0.41 V vs RHE. The donor density based on the wetted electrode surface of 5.7 cm^2 and the dielectric constant of 80 are 1.3 and 1.7 × 10^{20} cm^{-3}. It should be noted that no additional correction of the flatband potential is required due to this high donor density in contrast to the example reported by Boschloo et al.,[44] as the Helmholz capacitance was already accounted for in the fit of the space-charge capacitance with models b and c. A further estimation of V_{fb} was obtained with transient photo-

currents measurements. Chopped light gives rise to transient photocurrents, and the lowest anodic potential at which transients are observed is used as an indication of V_{fb}. Photocurrents measured with chopped white light resulted in a transient photocurrent onset at 0.4 V vs RHE for silicon-doped samples. This value lies close to the values determined from the Mott–Schottky curves obtained with models b and c.

Effective Surface Area. The nonlinear curves obtained by the Mott–Schottky analysis for the silicon-doped sample are similar in shape to the curves obtained for other highly doped nanostructures, most notably, the highly doped ZnO nanorods and nanoporous antimony-doped tin dioxide previously mentioned. This curvature can originate from two factors that decrease the active surface area contributing to the change in capacitance as a function of voltage: (1) complete depletion of the smallest feature sizes and (2) the curvature of the nanocrystal surface. To illustrate the first contribution, a sketch is presented in the right side of Figure 8 (sketches e–g). Here, the schematic that represented an electrode surface with different feature sizes in contact with the electrolyte is shown. As the electrode is biased in the anodic direction, the space-charge layer width, W, in the semiconductor is widened and the space-charge capacitance decreases. However, as W increases, the smallest sized features will become completely depleted and therefore no longer contribute to the decrease in capacitance. The electrode now resembles one with a smaller active surface area. Because C^{-2} is inversely proportional to the square of the effective surface roughness, a decrease in active surface area is a likely reason for the super linear Mott–Schottky curve. It is assumed that the surface roughness of 20, as determined by Orange II uptake,[24,49] with a surface occupation of 2.5 molecules nm^{-2} represents the surface roughness at low band bending.

Beside the full depletion of the smallest surface features, the effective electrode surface area could also be decreased by the curvature of the surface. Mora-Sero et al.[46] observed similarly shaped Mott–Schottky curves for the cylindrical rods of ZnO. Qualitatively, this result can be interpreted in terms of the effective surface area. An increasing space-charge layer width, W, reduces the capacitance, as they are inversely proportional. However, as the cylinders exhibit a concave surface with respect to the electrolyte, the effective surface area of the hypothetical plate capacitor is additionally decreased. This results in a more than proportional decrease in capacitance with increasing W,

Nanostructured Hematite Photoanodes

J. Phys. Chem. C, Vol. 113, No. 2, 2009 **781**

and thus a curved Mott–Schottky plot. Also, in this case the best approximation of the donor density comes from the slope at low band banding, as here the conditions of a flat plate capacitor are best approached. The effect of a curved surface is illustrated by sketch g in Figure 8, where the radius of the "inner plate" (in red) is reduced as compared to the radius of the "outer plate", r. As the width of the space-charge layer becomes much smaller than the radius of the feature, the situation of a flat surface is approached.

From the curvature of the Mott–Schottky data, it is possible to deduce the active surface area as function of the potential. For this purpose, an empirical relationship is fitted where the active surface area, A, is a function of the Schottky barrier voltage ($V - V_{fb}$):

$$A = A_0 + b(V - V_{fb}) \qquad (2)$$

Here, A_0 is set to 5.7×10^{-4} m^2 and represents the maximum surface area as determined by the dye adsorption and the geometric surface area. The proportionality factor, b, with units of m^2 V^{-1}, is a measure for the change of the active surface area as a function of applied potential. This relationship was substituted in the Mott–Schottky equation and fitted to the super linear Mott–Schottky plots in Figure 8 with a fixed value for A_0 of 5.7×10^{-4} m^2. A good fit was obtained with the proportionality factor for the curves for models b and c as -2.0×10^{-4} and -2.1×10^{-4} m^2 V^{-1}. This can be interpreted as a decrease of the active surface area by 35% at a bias voltage of 1 V positive of the flatband potential.

Donor Density of Undoped Film. The undoped film was fitted with a simple RC circuit (model a) between 39 and 79 kHz. In this frequency range, the slope of the imaginary impedance ranged between -1.01 and -1.05 in the voltage range, while the series resistance was constant ($22.3–22.9$ Ω). The capacitance fitted was much lower as compared to the doped sample and ranged between 0.199 and 0.187 μF for a bias range of $0.5–1.5$ V vs RHE and resulted in a flat Mott–Schottky curve with a slope of 1.81×10^{12} F^{-2} V^{-1}. Such a small slope is often reported when a semiconductor film interfaced with a conducting substrate is fully depleted; that is, the space-charge layer is limited by the thickness of the film.[50] As a consequence of this condition, the differential capacitance obtained from this film is attributed to the thin space-charge layer in the conducting substrate. A donor density that corresponds to the slope obtained for the undoped sample using the geometric surface area of 0.283 cm^2 and a dielectric constant of 10 reported for SnO$_2$[44] is 1×10^{20} cm^{-3}. This value matches well with the density reported for fluorine-doped SnO$_2$.[51,52] As the transmittance of the undoped sample is similar as compared to a doped sample with the same deposition time, it can be assumed that the film thickness of this sample is similar to that of the doped sample. Full depletion of film of 500 nm thickness can be obtained for a donor density in the order of 10^{16} and 10^{17} cm^{-3}, which is an acceptable value for undoped hematite.

Silicon Doping and Charge Separation. The results presented here and in our earlier work lead to the discussion of the dominant charge separation mechanism and the role that silicon plays in the improvement of the photocurrent in our mesoporous electrodes. As has been frequently reported,[7,8] the improved conductivity brought by the incorporation of the dopant is most likely from the n-type lattice substitution of Fe^{3+} by Si^{4+}, which results in a higher charge carrier concentration. We have previously reported a silicon content of 1.6 atom % vs Fe, which would correspond to a donor density of about 6×10^{20} cm^{-3} if all of the silicon is substitutionally incorporated in the lattice.[53]

This rough assumption agrees with the donor density calculated from the slope of the Mott–Schottky plot, as they are the same order of magnitude. The available density of states is estimated to be equal to the concentration of iron ions in the lattice (4×10^{22} cm^{-3}) corresponding to a nondegenerate semiconductor with a Fermi level positioned ca. 0.1 eV below the conduction band based on the electron occupancy of the conduction band.[54] An additional contribution to the conductivity can be expected from the preferential orientation of the (110) plane, which is induced by the presence of TEOS during the deposition.[22,24] This means that the most conductive crystal plane[55] is perpendicular toward the substrate when TEOS is added to the deposition gas, while this plane is randomly oriented in its absence. However, this anisotropic effect seems to be of minor importance as compared to silicon doping, as undoped photoanodes prepared by ultrasonic spray pyrolysis of similar thickness and the same preferred orientation of the (110) plane showed higher photocurrents for the back side than for the front side.[37] When silicon was added, the front side photocurrent increased above that of the backside, while the orientation was maintained.

Further, it has to be pointed out that the bulk of the photocurrent is generated in the fine-structured top section of the film with feature size commensurate to the hole diffusion length. Therefore, it would not be necessary to develop a space-charge layer to obtain a photocurrent as holes can diffuse to the surface to participate in the water oxidation reaction. Moreover, this would lead to the conclusion that charge separation is reaction-driven rather than driven by an electric field.[56,57] However, if the measured Si content of 1.6 atom % is indeed substitutionally incorporated in the lattice as suggested by the calculated donor density of around 10^{20} cm^{-3} from the Mott–Schottky plots (Figure 8), the formation of an electric field due to n-type doping can be responsible for the improved photocurrent. This is possible because the high charge carrier concentration compresses the width of the space-charge layer between 2 and 7 nm, which allows it to develop in the obtained feature size. If a lower fraction of the silicon is incorporated by Fe^{3+} substitution, a smaller contribution of the space charge to the charge separation is to be expected for films with appreciable stem widths as found in samples deposited for 5 min. Here, the stem width of about 100 nm allows for the development of a wider space-charge layer. However, because a space-charge layer in the 2–7 nm range is commensurate with the expected hole diffusion length in hematite, it is not possible to decouple the separate contributions of electric-field driven and diffusion driven carrier separation on the basis of the results presented. This interesting problem can be further addressed by preparing series of samples with various particle sizes and known doping concentrations.

4. Conclusion

The investigations we have presented here with APCVD hematite photoanodes for solar water splitting show the many complexities of this system. Thin-film formation is characterized by linear growth with an incubation time. Porous dendritic structures develop from a delicate interaction of homogeneous particle nucleation in the precursor gas stream and substrate-based attachment and growth. The observed feature sizes of the film depend on substrate temperature and the presence of silicon precursor (TEOS). This, in turn, has a strong effect on the observed crystalline disorder (shown via the Raman band at 660 cm^{-1}) and ultimately on the solar photocurrent and the quantum efficiency (APCE), the optimal photoresponse being obtained from films with feature sizes of about twice the reported

782 *J. Phys. Chem. C, Vol. 113, No. 2, 2009*

Cesar et al.

hole diffusion length (5 nm). We have also presented evidence for an unusually high donor density on the order 10^{20} cm^{-3}, which would allow the formation of a space-charge field inside the nanosized features of the polycrystalline hematite photoanode, a factor that could play a major role in the separation of charges and enhancement of performance, even in the surface features of 5 nm. This suggests that high doping density could be an important design strategy for solar water splitting by nanostructured photoelectrodes. Further, through our studies varying the film thickness, we have shown that the silicon doping enables electron transport from the top of the film to the substrate up to a distance of at least 600 nm. However, this work also led to the discovery of a higher recombination rate of photogenerated carriers in the section of the hematite film near the fluorine doped tin oxide, as compared to the bulk section of the film. This "dead layer" and the disaccord between the photon penetration depth and the hole diffusion length keep the quantum efficiency of these dendritic photoanodes low as compared to similar materials and provides continued challenges for obtaining the full potential of hematite photanodes for water splitting.

References and Notes

(1) Fujishima, A.; Honda, K. *Nature* **1972**, *238*, 37.

(2) Gratzel, M. *Nature* **2001**, *414*, 338.

(3) Based on an integrated solar photocurrent below 610 nm and an upper heating value for hydrogen combustion of−280 kJ/mol or 1.45 eV/electron.

(4) Kennedy, J. H.; Frese, K. W. *J. Electrochem. Soc.* **1978**, *125*, 709.

(5) Ghosh, A. K.; Maruska, H. P. *J. Electrochem. Soc.* **1977**, *124*, 1516.

(6) Sanchez, C.; Sieber, K. D.; Somorjai, G. A. *J. Electrochem. Soc.* **1988**, *252*, 269.

(7) Kennedy, J. H.; Frese, K. W. *J. Electrochem. Soc.* **1978**, *125*, 723.

(8) Shinar, R.; Kennedy, J. H. *Sol. Energy Mater. Sol. Cells* **1982**, *6*, 323.

(9) Leygraf, C.; Hendewerk, M.; Somorjai, G. *J. Solid State Chem.* **1983**, *48*, 357.

(10) Harry, O. F. *Semiconductor Electrodes*; Elsevier: Amsterdam, 1988.

(11) Morrision, S. R. *Electrochemistry at Semiconductor and Oxidized Metal Electrodes*, 1st ed.; Plenum Press: New York, 1980.

(12) Gardner, R. F. G.; Tanner, D. W.; Sweett, F. *J. Phys. Chem. Solids* **1963**, *24*, 1183.

(13) Tomkiewicz, M.; Fay, H. *J. Appl. Phys.* **1979**, *18*, 1.

(14) Based on a 1 V Schottky barrier and a dielectric constant of 80.

(15) Kennedy, J. H.; Anderman, M.; Shinar, R. *J. Electrochem. Soc.* **1981**, *128*, 2371.

(16) Itoh, K.; Bockris, J. O. *J. Electrochem. Soc.* **1984**, *131*, 1266.

(17) Quinn, R. K.; Nasby, R. D.; Baughman, R. J. *Mater. Res. Bull.* **1976**, *11*, 1011.

(18) Itoh, K.; Bockris, J. O. *J. Appl. Phys.* **1984**, *56*, 874.

(19) Ribeiro, C.; Lee, E. J. H.; Giraldi, T. R.; Aguiar, R.; Longo, E.; Leite, E. R. *J. Appl. Phys.* **2005**, *97*, 024313.

(20) Bjorksten, U.; Moser, J.; Gratzel, M. *Chem. Mater.* **1994**, *6*, 858.

(21) Lindgren, T.; Wang, H. L.; Beermann, N.; Vayssieres, L.; Hagfeldt, A.; Lindquist, S. E. *Sol. Energy Mater. Sol. Cells* **2002**, *71*, 231.

(22) Cesar, I.; Kay, A.; Martinez, J. A. G.; Gratzel, M. *J. Am. Chem. Soc.* **2006**, *128*, 4582.

(23) Duret, A.; Gratzel, M. *J. Phys. Chem. B* **2005**, *109*, 17184.

(24) Kay, A.; Cesar, I.; Gratzel, M. *J. Am. Chem. Soc.* **2006**, *128*, 15714.

(25) Santato, C.; Ulmann, M.; Augustynski, J. *J. Phys. Chem. B* **2001**, *105*, 936.

(26) NREL AM 1.5 Gobal solar spectrum derived from SMARTS v. 2.9.2; http://rredc.nrel.gov/solar/spectra/am1.5/.

(27) Seaman, C. H. *Sol. Energy* **1982**, *29*, 291.

(28) Bersani, D.; Lottici, P. P.; Montenero, A. *J. Raman Spectrosc.* **1999**, *30*, 355.

(29) Orthner, H. R.; Roth, P. *Mater. Chem. Phys.* **2002**, *78*, 453.

(30) Montassier, N.; Boulaud, D.; Renoux, A. *J. Aerosol Sci.* **1991**, *22*, 677.

(31) Zheng, F. *Adv. Colloid Interface Sci.* **2002**, *97*, 255.

(32) Sartoretti, C. J.; Ulmann, M.; Alexander, B. D.; Augustynski, J.; Weidenkaff, A. *Chem. Phys. Lett.* **2003**, *376*, 194.

(33) Zboril, R.; Mashlan, M.; Petridis, D. *Chem. Mater.* **2002**, *14*, 969.

(34) Sartoretti, C. J.; Alexander, B. D.; Solarska, R.; Rutkowska, W. A.; Augustynski, J.; Cerny, R. *J. Phys. Chem. B* **2005**, *109*, 13685.

(35) McCarty, K. F. *Solid State Commun.* **1988**, *68*, 799.

(36) Morl, K.; Ropke, U.; Knappe, B.; Lehmann, J.; Perthel, R.; Schroder, H. *Thin Solid Films* **1979**, *60*, 49.

(37) Cesar, I. *Solar Photoelectrolysis of Water with Translucent Nanostructured Hematite Photoanodes*; EPFL: Lausanne, 2007.

(38) Benko, F. A.; Koffyberg, F. P. *Mater. Res. Bull.* **1986**, *21*, 1183.

(39) Iwanski, P.; Curran, J. S.; Gissler, W.; Memming, R. *J. Electrochem. Soc.* **1981**, *128*, 2128.

(40) Liang, Y. Q.; Enache, C. S.; van de Krol, R. *Int. J. Photoenergy* **2008**, 739864.

(41) Peter, L. M. *Chem. Rev.* **1990**, *90*, 753.

(42) Glasscock, J. A.; Barnes, P. R. F.; Plumb, I. C.; Bendavid, A.; Martin, P. J. SPIE International Symposium on Optics & Photonics: Solar Hydrogen and Nanotechnology (SE442); San Diego, CA, 2006; p 12.

(43) Dareedwards, M. P.; Goodenough, J. B.; Hamnett, A.; Trevellick, P. R. *J. Chem. Soc., Faraday Trans. 1* **1983**, *79*, 2027.

(44) Boschloo, G.; Fitzmaurice, D. *J. Phys. Chem. B* **1999**, *103*, 3093.

(45) Benko, F. A.; Longo, J.; Koffyberg, F. P. *J. Electrochem. Soc.* **1985**, *132*, 609.

(46) Mora-Sero, I.; Fabregat-Santiago, F.; Denier, B.; Bisquert, J.; Tena-Zaera, R.; Elias, J.; Levy-Clement, C. *Appl. Phys. Lett.* **2006**, *89*, 203117.

(47) Horowitz, G. *J. Electroanal. Chem.* **1983**, *159*, 421.

(48) Degryse, R.; Gomes, W. P.; Cardon, F.; Vennik, J. *J. Electrochem. Soc.* **1975**, *122*, 711.

(49) Bandara, J.; Mielczarski, J. A.; Kiwi, J. *Langmuir* **1999**, *15*, 7670.

(50) vandeKrol, R.; Goossens, A.; Schoonman, J. *J. Electrochem. Soc.* **1997**, *144*, 1723.

(51) Rakhshani, A. E.; Makdisi, Y.; Ramazaniyan, H. A. *J. Appl. Phys.* **1998**, *83*, 1049.

(52) Thangaraju, B. *Thin Solid Films* **2002**, *402*, 71.

(53) Based on a density of 5.28 g cm^{-3} and a molar weight of 160 g mol^{-1} for Fe$_2$O$_3$.

(54) Nozik, A. J.; Memming, R. *J. Phys. Chem.* **1996**, *100*, 13061.

(55) Iordanova, N.; Dupuis, M.; Rosso, K. M. *J. Chem. Phys.* **2005**, *122*, 144305.

(56) Bard, A. J. *J. Phys. Chem.* **1982**, *86*, 172.

(57) Hodes, G.; Howell, I. D. J.; Peter, L. M. *J. Electrochem. Soc.* **1992**, *139*, 3136.

JP809060P